Basin Modes in a Tropical–Extratropical Basin[*]

Haijun Yang

Department of Atmospheric Science, School of Physics, Peking University, Beijing, China

Zhengyu Liu

Center for Climatic Research and Department of the Atmospheric and Oceanic Sciences, University of Wisconsin—Madison, Madison, Wisconsin

ABSTRACT

The full spectrum of basin modes in a tropical–extratropical basin is studied comprehensively in a linear shallow-water system. Two sets of least-damped basin modes are identified. At the low-frequency end is the planetary wave basin mode, whose period is determined by the cross-basin time of the planetary wave on the poleward boundary of the basin, consistent with recent theories. At the higher-frequency end is the Kelvin wave basin mode, whose period is determined by the around-basin traveling time of the Kelvin wave. Sensitivity experiments are also performed on the eigenvalue problem to study the dynamics of these basin modes. It is found that the period of the planetary wave basin mode is determined by an effective basin boundary that is always at a latitude no higher than the geometric basin boundary. The effective poleward boundary is located at the most poleward latitude where the planetary wave can cross the entire basin. It is also found that the Kelvin wave basin modes are vulnerable to boundary perturbations. If the coastal Kelvin wave propagation is suppressed along the basin boundary, the Kelvin wave basin mode would degenerate to the equatorial basin mode that has been obtained theoretically from the long-wave approximation.

1. Introduction

Previous theories have identified some low-frequency basin modes in a tropical–extratropical ocean basin. Focusing on the equatorial region and using classical equatorial wave dynamics (Moore 1968), Cane and Moore (1981, CM hereinafter) have theoretically identified a set of slightly leaky equatorial basin (EB) modes formed by the reflection of equatorial Kelvin and Rossby waves in the equatorial waveguide. The gravest EB mode has a period of 4 times the traveling time of the equatorial Kelvin wave across the basin, ranging from seasonal to interannual timescales. By solving the same equatorial wave equations theoretically under the long-wave approximation, Jin (2001) found a set of very low frequency (VLF) modes with periods of decadal and interdecadal timescale. These VLF modes are distinctly different from the EB mode, not only in the frequencies but also in the spatial structures. The VLF modes are featured with a zonal uniformly deepening and shoaling

of the equatorial thermocline, which can be understood as the free heat-content recharge oscillations.

Focusing on the midlatitude region and using classical planetary wave dynamics, Cessi and Louazel (2001, CL hereinafter) and Cessi and Primeau (2001) identified a set of weakly damped planetary wave basin (PB) modes. These PB modes are formed by the interaction of extratropical planetary waves and coastal Kelvin waves, exhibiting periods of interannual to interdecadal timescales. Liu (2002, LIU hereinafter) further showed that the PB mode is also the lowest-frequency basin mode and therefore determines the longest memory of a tropical–extratropical basin. These PB modes are very weakly damped, even in the presence of dissipation such that they could be easily resonantly excited (Primeau 2002; Liu 2003).

All these previous works have used approximate analytical models. Furthermore, they have focused either on the EB mode or the PB mode. Naturally, this prompts the questions: Do these modes exist in the full spectrum of the basin modes of a unified shallow-water system? Furthermore, are there other new modes? This paper attempts to improve understanding of the basin modes in a tropical–extratropical basin. Our motivations are twofold: first, to investigate all the least-damped basin modes in a tropical–extratropical basin in a compre-

---

Corresponding author address: Haijun Yang, Department of Atmospheric Science, School of Physics, Peking University, Beijing, China 100871.
E-mail: mikey@navyang.com

TABLE 1. Typical parameters for the control case in the linear shallow-water model.

Symbol	Value	Parameter
g'	0.02 m s^{-2}	Reduced gravity
β	1.98×10^{-11} m^{-1} s^{-1}	Meridional gradient of Coriolis parameter
D	400 m	Mean depth for upper ocean
r_u	8×10^{-7} s^{-1}	Oceanic Rayleigh friction for u equation
r_v	8×10^{-7} s^{-1}	Oceanic Rayleigh friction for v equation
r_h	0	Newtonian damping for h equation
δ_u	0.107	$r_u/(\beta L_d)$, nondimensional form of r_u
δ_v	0.107	$r_v/(\beta L_d)$, nondimensional form of r_v
c_0	2.83 m s^{-1}	Oceanic gravity wave speed
ρ_0	1.0×10^3 kg m^{-3}	Density of ocean water
L_d	378 km	Equatorial deformation radius
L_x	3000 km	Basin zonal extension
L_y	5000 km	Basin meridional extension
M	7.94	L_x/L_d, ratio of L_x and L_d

hensive way and, second, to further explore the dynamics and the formation mechanisms of each basin mode.

In this paper, the full spectrum of basin modes is obtained numerically by solving the finite difference eigenvalue problem of a linear shallow-water system on a finite equatorial beta plane. At the low-frequency end, the PB mode is studied extensively. The PB mode has the period determined by the cross-basin time of the planetary wave on the poleward basin boundary. At the high-frequency end, the Kelvin wave basin (KB) mode is identified. The frequency of KB mode is determined by the Kelvin wave traveling time around the basin. The EB mode that was derived theoretically by CM cannot be identified in the spectrum for the full shallow-water equations on a finite beta plane. Instead, the EB mode stands out under the long-wave approximation or with heavy extratropical boundary damping. It appears to be the degenerate KB mode when the propagation of the coastal Kelvin wave is suppressed.

This paper is arranged as follows. The model and the numerical method are described in section 2. The dynamics of the PB, KB, and EB modes are studied in sections 3, 4, and 5, respectively. Section 6 summarizes the main conclusions and provides some further discussions.

2. The model

A linear 1.5-layer model for the upper-ocean dynamics in a tropical–extratropical basin is used in this paper. A rectangular basin is considered with $0 \leq y \leq L_y$ and $0 \leq x \leq L_x$. On the equatorial beta plane and with linear damping, the shallow-water system can be written as (e.g., CM; CL)

$$u_t - yv + h_x + M\delta_u u = 0, \quad (1a)$$

$$v_t + M^2(yu + h_y) + M\delta_v v = 0, \quad \text{and} \quad (1b)$$

$$h_t + u_x + v_y + M\delta_h h = 0. \quad (1c)$$

This system has been nondimensionalized by the equatorial deformation radius $L_d = (c_0/\beta)^{1/2}$ for y, the basin

width L_x for x, the Kelvin wave crossing time L_x/c_0 for t, the mean depth D for h, and the Kelvin wave speed c_0 and $c_0 L_d/L_x$ for u and v, respectively. Here β is the meridional gradient of Coriolis parameter, $c_0 = (g'D)^{1/2}$, where g' is the reduced gravity; $M = L_x/L_d$ is the ratio of the basin zonal scale and the equatorial deformation radius; and $\delta_u = r_u/\beta L_d$, $\delta_v = r_v/\beta L_d$, and $\delta_h = r_h/\beta L_d$ are nondimensional linear damping coefficients. For a rectangular basin of $L_x = 3000$ km and $L_y = 5000$ km, the nondimensional basin becomes $X = [0, 1]$ and $Y = [0, 13.238]$.

The boundary conditions used are the no-normal flow condition on the basin boundaries, which implies the conservation of the total mass (when $\delta_h = 0$) as

$$\frac{\partial}{\partial t}\left(\int_0^{L_x} \int_0^{L_y} h \, dy \, dx\right) = 0. \quad (2)$$

Assuming the eigensolution of the form:

$$\begin{pmatrix} u \\ v \\ h \end{pmatrix} = e^{-i\sigma t} \begin{pmatrix} \hat{u} \\ \hat{v} \\ \hat{h} \end{pmatrix}(x, y), \quad (3)$$

we have the eigenvalue problem (also see CL):

$$i\sigma \begin{pmatrix} \hat{u} \\ \hat{v} \\ \hat{h} \end{pmatrix} \begin{pmatrix} M\delta_u & -y & \partial_x \\ M^2 y & M\delta_v & M^2\partial_y \\ \partial_x & \partial_y & M\delta_h \end{pmatrix} \begin{pmatrix} \hat{u} \\ \hat{v} \\ \hat{h} \end{pmatrix} = \mathsf{L} \begin{pmatrix} \hat{u} \\ \hat{v} \\ \hat{h} \end{pmatrix}, \quad (4)$$

where σ is the eigenvalue and L is derived from the shallow-water equations and the no-normal flow boundary condition. The eigenvalue σ and eigenvector (u, v, h) are determined numerically by approximating L with a finite-difference C grid (appendix A). Unless otherwise specified, our solutions are obtained in a rectangular basin with the typical parameters listed in Table 1.

In this paper, the least-damped basin modes that have large spatial scale and seasonal to decadal timescales are examined. Figure 1 shows the eigenvalue spectrum in the frequency range of 0.03–400 cycles per year (cpy) in the control case whose parameters are given in Table
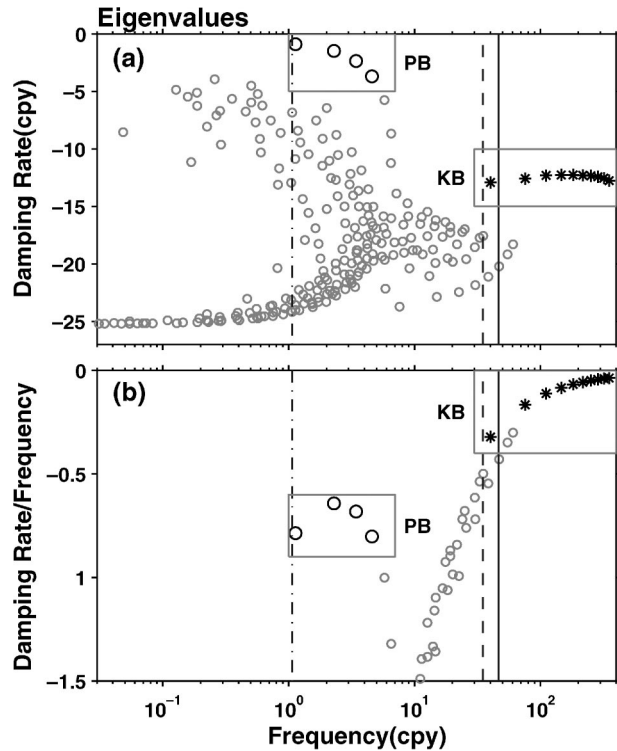
FIG. 1. Scatterplot of the eigenvalues, $\sigma = \lambda + i\omega$, obtained by solving (4) numerically with the standard parameters listed in Table 1. In (a) the y coordinate represents damping rate λ while in (b) it represents the ratio of damping rate λ to frequency ω. The logarithmic coordinate is adopted in the x coordinate. The unit of the frequency and damping rate is cycles per year (cpy). The first few PB and KB modes are outlined in light-lined rectangular boxes and highlighted by dark circles and asterisks, respectively. The dash–dotted line, dashed line, and solid line in (a) and (b) label the frequencies of the first PB, KB, and EB modes estimated from theory, respectively.

1. Two sets of least-damped basin modes stand out, one of which has very low frequencies (1–10 cpy) (heavy circles). These are the PB modes that were first identified by CL and will be studied further in section 3. Notice that at the low-frequency regime there are many additional modes, some of which are probably numerical modes rather than physical modes. These additional low-frequency modes, however, are much more heavily damped than the PB modes. Furthermore, their damping rates are much faster than their frequencies (Fig. 1b), consequently, exhibiting an oscillatory nature far more subdued than the PB modes.

Toward higher frequencies (between 40 and 400 cpy) another set of least-damped modes stands out (heavy asterisks in Fig. 1). These modes have larger absolute damping rates than the PB modes; however, their frequencies are much higher such that the ratios of damping rates to frequencies are much smaller than those of PB modes (Fig. 1b). Therefore, they exhibit an enhanced oscillatory nature in comparison with the PB modes. These modes will be shown to be the KB modes in section 4.
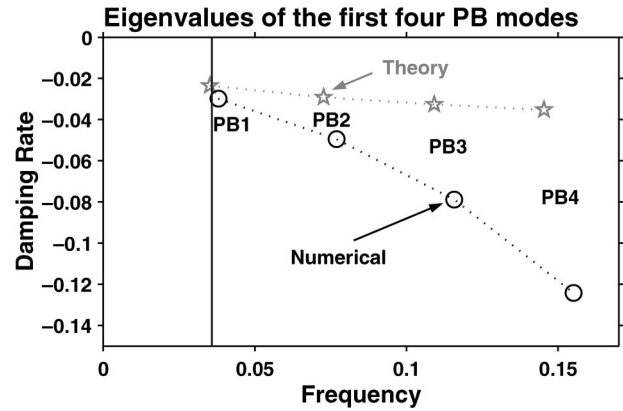

FIG. 2. Eigenvalues of the first four PB modes obtained from our model (dark circles) and theory (light stars) for a basin of 3000 km $\times$ 5000 km. The eigenvalues have been nondimensionalized by c_0/L_x, where c_0 is the Kelvin wave speed and L_x is the zonal extension of the basin. The solid line labels the frequency of the first theoretical PB mode ω_{P1}. The damping rates of the numerical modes are larger than those of the theoretical modes because of realistic damping coefficients incorporated into the numerical model.

3. Planetary wave basin modes

a. The PB modes

It has been shown that the nth PB mode has the frequency $\omega_{Pj} = j\omega_{P1}$, where ω_{P1} is the frequency of the gravest PB mode (Jin 2001; CL; LIU; also see appendix B), given as

$$\omega_{P1} = 2\pi/Y_N^2. \tag{5}$$

This fundamental frequency ω_{P1} corresponds to the cross-basin time of the planetary wave along the northern boundary $Y_N (L_y/L_d)$. Figure 2 shows the eigenvalues of the first four PB modes derived from theory (stars) and the finite-difference system (circles) in a basin of $Y_N = 5000$ km/L_d. The numerical solutions agree well with the theoretical solutions. The numerical modes are seen to have somewhat larger damping rates, especially for higher PB modes, because of the explicit momentum damping present in the numerical model. The structures of the PB modes are also consistent with the theoretical solutions as shown in Fig. 3, which only shows the real part of the first two PB modes. For example, the amplitude increases toward the northwest corner and the zonal wavenumber is one (two) along the northern boundary for mode one (two). In addition, there is no node point along the equator. It bears noting that the PB modes in Fig. 3 are very similar to the VLF modes shown in Jin (2001): especially in the Tropics, they all have zonally uniform equatorial thermocline, suggesting that they have the same physical nature (LIU).

The period of the PB modes increases with the poleward shift of the northern boundary of the basin (LIU). Figure 4a shows that the frequency of the first two PB modes decreases when the northern boundary Y_N increases from about 2000 to 8000 km. Furthermore, the

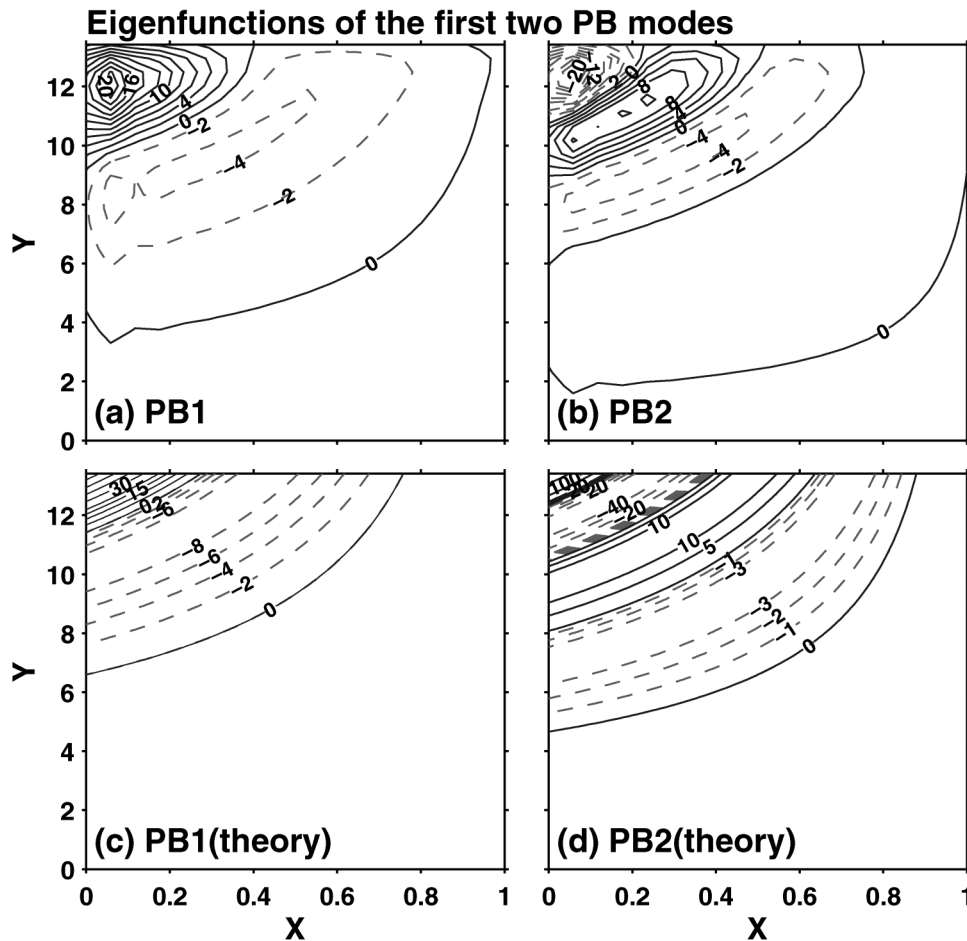**Eigenfunctions of the first two PB modes**

FIG. 3. Eigenstructures (real part of H) of the first two PB modes obtained from (a), (b) our model and (c), (d) theory: (a) and (c) show the first mode, and (b) and (d) show the second mode. The nondimensional eigenvalues are (a) $-0.029 + i0.038$, (b) $0.049 + i0.077$, (c) $-0.024 + i0.036$, and (d) $-0.029 + i0.072$. The basin size has been normalized by L_x in the zonal and L_d in the meridional directions.

frequency is proportional to $1/Y_N^2$, such that it remains almost constant after being normalized by the fundamental frequency ω_{P1} (Fig. 4b).

b. Formation mechanism

The formation mechanism of PB modes can be easily understood from the basin adjustment process studied by Liu et al. (1999) (also CL, LIU). When an initial planetary wave hits the western boundary, the mass of the wave is quickly transferred back to the eastern boundary via a coastal Kelvin wave along the western basin boundary and an equatorial Kelvin wave along the equator, and is then radiated westward by a secondary planetary waves generated along the eastern boundary. Since the planetary wave speed varies with latitude, the PB mode decays because of the distortion of the wave front after each reflection upon the western boundary, even in the absence of explicit dissipation in the interior ocean.

Coastal Kelvin waves along the basin boundaries

could be crucial for the establishment of the PB mode (Milliff and McWilliams 1994). In the eigenvalue problem, the role of wave propagation can be demonstrated in experiments in which an excessively large damping is imposed in the Eqs. (1a)–(1c) in a specific "damping region" (see appendix A). First, Kelvin wave propagation is suppressed along the eastern boundary by applying an excessive damping there. The PB modes disappear as shown in the eigenvalue spectrum in Fig. 5. The results are similar when the damping is applied on the western boundary (not shown). These experiments suggest that the coastal Kelvin waves along the eastern and western boundaries are critical for the PB modes. In contrast, when the damping region is applied along the northern boundary, the PB modes (not shown) remain almost identical to the control case in Fig. 1, suggesting that the coastal Kelvin wave on the northern boundary is unimportant for the PB mode. The role of coastal Kelvin waves above can be understood from the basin adjustment viewpoint (Liu et al. 1999), whereby the suppression of coastal Kelvin waves along the east-
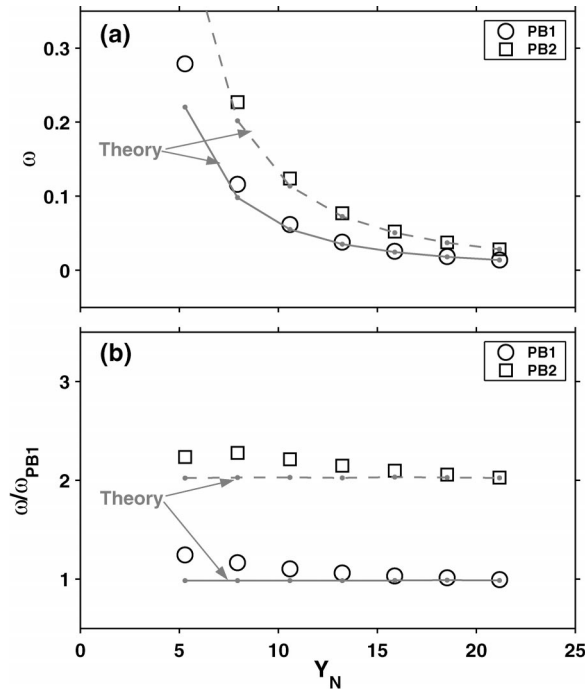
FIG. 4. Eigenfrequencies of the first two numerical PB modes (circles for first mode and squares for second mode) for different northern boundaries Y_N. In (b) the frequencies have been normalized by the fundamental frequency ω_{P1}. The theoretical first (dot–solid line) and second (dot–dashed line) PB modes are also plotted for comparison. The numerical modes coincide with the theoretical ones very well, especially with larger Y_N.
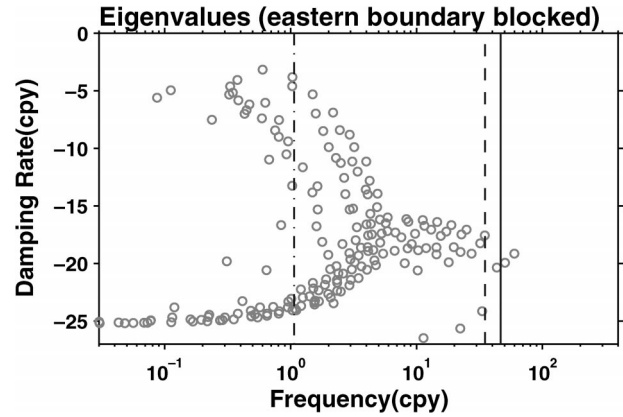

FIG. 5. As in Fig. 1a but for the basin where the excessive damping is applied along the whole eastern boundary. There are no isolated PB and KB modes because of eastern boundary blocking.

ern or western boundary cut off the mass redistribution route towards the eastern boundary. As a result, no secondary planetary waves are generated from the eastern boundary, yielding no response in the interior ocean. Therefore, the PB mode disappears. On the contrary, the northern boundary Kelvin wave does not contribute to the excitation of planetary waves along the eastern boundary and therefore has no impact on the PB mode.

It is important to point out that the period of the PB mode depends on an "effective northern boundary" rather than the geometric northern boundary. The effective northern boundary is the northernmost latitude that the eastern boundary Kelvin wave can reach (LIU). This can be demonstrated here by applying a damping region along a portion of the eastern boundary. Figure 6 shows the eigenvalue spectrum in the low frequency regime (upper panels) and the structures of the corresponding first PB modes (lower panels) in several different cases of partially blocked eastern boundary. In the control case of no damping along the eastern boundary, the first PB mode has the frequency $\omega_{P1} = 2\pi/Y_N^2$ (Fig. 6a) and the structure with amplitude increasing toward the basin's northwest corner (Fig. 6b), as discussed in Figs. 1 and 3. When the damping region occupies the northern quarter of the eastern boundary to $3Y_N/4$ (shaded region in Fig. 6d), the frequency of the first PB mode increases to $\omega_{P1} = 2\pi/(3Y_N/4)^2$ (Fig. 6c).

If the damping region is further extended to occupy the northern half of the eastern boundary to $Y_N/2$ (Fig. 6f), the frequency of the first PB mode further increases to $\omega_{P1} = 2\pi/(Y_N/2)^2$ (Fig. 6e). Therefore, the effective northern boundary becomes $3Y_N/4$ and $Y_N/2$ in Figs. 6c and 6e. The structure of the first PB mode is also determined mainly by the effective northern boundary, as seen in Figs. 6d and 6f, where the amplitude of the first PB mode increases towards the northwest corner of the effective basin rather than the geometric basin. The zonal wavenumber-one structure also shows up clearly along the effective northern boundary, and not the geometric northern boundary (Figs. 6d,f). The amplitude north of the effective northern boundary is always small.

Since the PB mode depends critically on the passing of the eastern boundary planetary waves, one can further speculate that the effective northern boundary of the PB mode is the southernmost latitude where the planetary wave can travel across the entire basin. This is demonstrated by the experiment illustrated in Figs. 6g,h. In this case, a damping region is applied to the middle of the basin extending to the latitude of $Y_N/2$. The eigenvalues in Fig. 6g are almost identical to the half eastern boundary blocking case in Fig. 6e, while the first PB modes also exhibit similar structures in both cases (Figs. 6f,h). This is easy to understand since both cases have the southern tip of damping region at $Y_N/2$, corresponding to the southernmost latitude where the planetary wave can cross the basin and therefore is the effective northern boundary for the PB modes.

In short, the formation of PB modes is critically dependent upon the wave propagation processes along the basin boundaries except the northern boundary. Furthermore, the PB modes are determined by the effective northern boundary rather than the geometric northern boundary.

4. Kelvin wave basin modes

In Fig. 1, a series of least-damped modes at the higher-frequency regime (asterisks) are noted. These basin modes
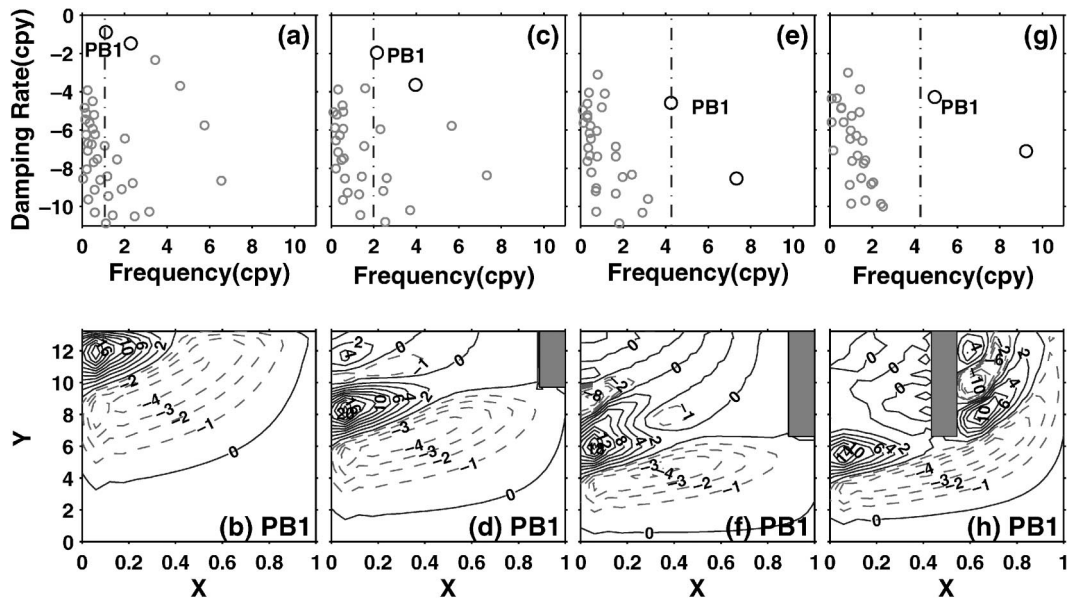
FIG. 6. Scatterplot of the (upper) eigenvalues and the eigenstructures (real part of H) of the (lower) first PB modes for the basins with different partially blocked boundary. Panels (a) and (b) are for the control case. In (d), (f), and (h), the light-shadowed regions specify the extreme damping region. The first and second PB modes in (c), (e), and (g) are highlighted by dark circles.

are, somewhat unexpectedly, not the same as the EB mode of CM. Instead, these higher-frequency basin modes are the so-called Kelvin wave basin modes, or KB modes. The period of the gravest KB mode is equal to the travel time of the Kelvin wave along the basin perimeter and can be written in the nondimensional form as

$$\sigma_{K1} = 2\pi \frac{L_x}{L_p} = \frac{\pi}{1 + Y_N/M}, \qquad (6a)$$

where $L_p = 2L_x + 2L_y$ is the perimeter of the basin and $M = L_x/L_d$. The nth KB mode has a frequency of

$$\sigma_{Kj} = j\sigma_{K1}. \qquad (6b)$$

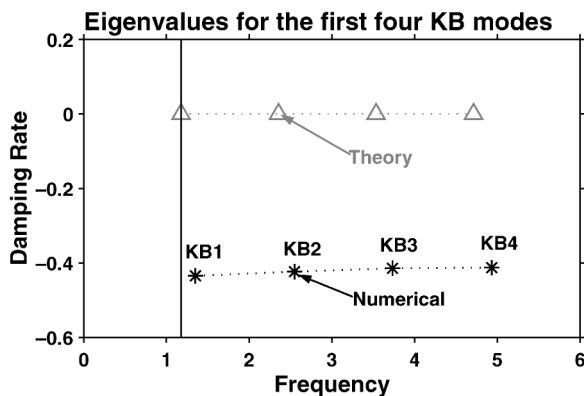Figure 7 shows the eigenvalues of the first four KB

FIG. 7. As in Fig. 2 but for the first four KB modes from numerical model (dark asterisks) and theory (light triangles). The solid line labels the frequency of the first theoretical KB mode.

modes from the standard solution (Fig. 1a). The numerical solutions agree well with the theoretical estimate based on (6a,b). Relative to the frequencies, the damping rates of KB modes are very small and nearly constant.

The spatial structure of the KB mode is characterized by an amplitude trapped within about one deformation radius from the boundary and the equatorial waveguide. This can be seen for the first and second KB modes in Fig. 8. The trapping along the coastal boundaries is consistent with the propagation of the coastal Kelvin wave. However, the broad amplitude in the equatorial waveguide, especially for the first KB mode (Fig. 8a), suggests a possible involvement of equatorial Rossby wave, a point to be discussed later. In general, along the basin perimeter, the nth KB mode has the wavenumber n and node point $2n$ (Fig. 9). The x axis in Fig. 9 represents the distance counterclockwise along the western, southern, eastern, and northern boundaries of the basin. The along-boundary values of the real part of the eigenfunctions are plotted for the first four KB modes. It is seen that the first KB mode corresponds to wavenumber one and has two node points around the basin; the second KB mode corresponds to the wavenumber two and has four node points, and so on.

The frequencies of the KB modes decrease with increasing basin size. For example, for a fixed L_x, the frequency of the first KB mode decreases from 2.8 to 1.1 when Y_N increases from about 1000 to 8000 km (Fig. 10a). For a fixed Y_N, the frequency of the first KB mode decreases from 1.9 to 0.9 when L_x increases from 1000 to 6000 km (Fig. 10b). These frequencies well
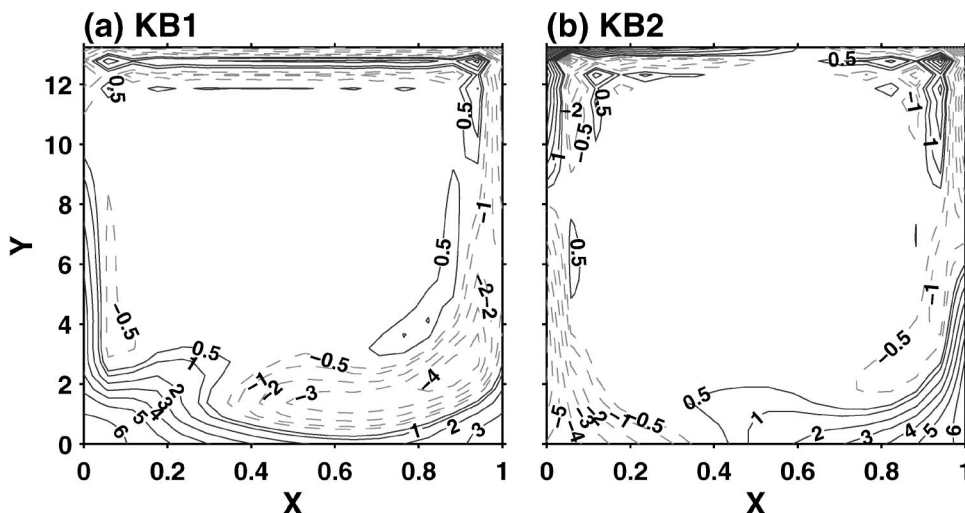
FIG. 8. Eigenstructures (real part of H) of the (a) first and (b) second numerical KB modes. The basin size has been normalized by L_x in the zonal and L_d in the meridional directions.

agree with the theoretical estimates (Figs. 10a,b). Similar conclusions can be drawn for the second and other KB modes.

Since the KB modes are established by the Kelvin waves traveling around the basin, one can speculate that the KB modes could easily be suppressed if the propagation of coastal Kelvin wave is suppressed somewhere along the boundary. This can indeed be seen in the previous example in Fig. 5, in which the coastal Kelvin waves are suppressed along the entire eastern boundary. Under this situation, all the KB modes disappear (as are the PB modes as discussed in the previous section). Similarly, all the KB modes are suppressed by any part of the boundary damping. Even in the case of northern boundary damping (Figs. 6g,h) where the PB modes are

FIG. 9. Eigenstructures (real part of H) of the first four numerical KB modes along the basin boundaries. The x coordinate shows the grid numbers, which represent the distance counterclockwise along the basin boundaries, starting from the northernmost grid point on western boundary. The W, S, E, and N represent the western, southern, eastern, and northern boundaries, respectively. The square, dot, circle, and cross lines are for the first, second, third, and fourth KB mode, respectively.

not affected, the KB modes are eliminated. This is because the coastal Kelvin wave propagation along the northern boundary, although unimportant for the PB modes, is of the same importance of coastal Kelvin wave on other boundaries to the KB modes. The strong sensitivity of the KB modes to boundary Kelvin waves suggests that the KB modes may not be very robust in a realistic ocean that has a basin boundary consisting of complex continental shelves and open straits, because to some extent those kinds of geometry act like strong boundary damping to obstruct the coastal Kelvin wave.

5. Equatorial basin modes

It is somewhat unexpected that our basin mode calculation does not produce the EB mode of CM. This is not necessarily in contradiction to previous results because so far all the EB modes have been derived only in theoretical models after the long-wave approximation (CM; Jin 2001). No previous works have shown the presence of EB modes in the full shallow-water equation (1). Nonetheless, Fig. 8 shows that most of the energy of the KB mode, especially the first KB mode, is confined within the equatorial waveguide, with only a relatively small part of the wave energy "leaking out" into higher latitudes (presumably by the eastern boundary Kelvin wave). This suggests that the KB mode may be related to the EB mode. This is indeed the case as shown below.

After the long-wave approximation, CM derived the EB mode analytically on an infinite equatorial beta plane. It is shown that the frequency for the gravest EB mode is $\omega_{E1} = \pi/2$ (see appendix B for details) and for a higher EB mode becomes $\omega_{Ej} = j\pi/2$, with j being the number of node points on the equator. These EB modes can indeed be reproduced in the numerical model after the long-wave approximation (appendix A) as
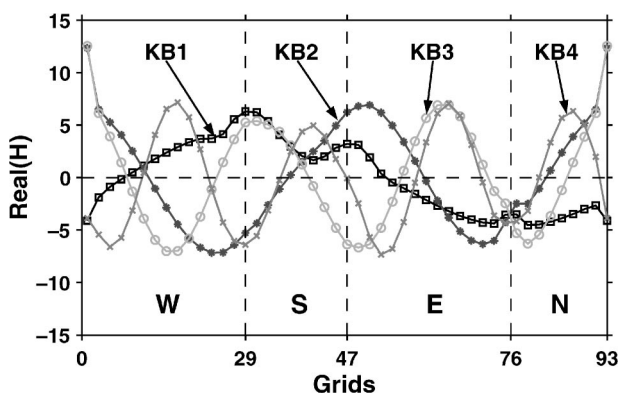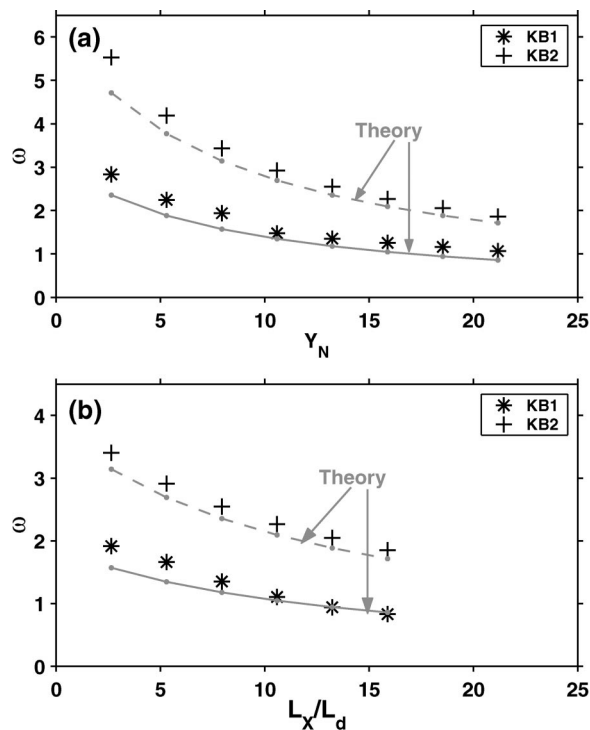
FIG. 10. Eigenvalues of the first two numerical KB modes (asterisks for the first mode and pluses for the second mode) for (a) different northern boundary Y_N and (b) different basin length L_x. In (b), the frequencies have been divided by L_x/L_{x0}, where $L_{x0} = 3000$ km is the basin length in the control case. The first (dot–solid line) and second (dot–dashed line) theoretical KB modes are also plotted for comparison.

shown by the heavy crosses in Fig. 11c. It is interesting to see that these EB modes can also be reproduced in the experiment in which the Kelvin waves are suppressed along the northern boundary (dark pluses in Fig. 11b). The KB modes that were originally identified in the control case (dark asterisks in Fig. 11a, or Fig. 1) are now eliminated (Fig. 11b). In this case, the Kelvin

wave is suppressed along the northern boundary such that the coastal Kelvin wave can no longer circulate around the basin. The KB modes can therefore no longer be formed. Nonetheless, the poleward energy due to the coastal Kelvin wave along the eastern boundary can be reflected by the westward equatorial Rossby waves in the equatorial waveguide. This equatorial Kelvin and Rossby wave reflection establishes the EB mode, as discussed by CM.

Further examinations of similar patterns of the first KB mode (Fig. 8a) and the first EB mode (Figs. 12b,c) in the Tropics confirm that the EB modes are degenerated from the KB modes. Both the KB and EB modes have maximum amplitudes confined within the equatorial waveguide and a signature of eastern boundary reflection. The only major difference is that the first EB mode has a clear node point on the equator whereas the first KB mode does not. The patterns of the numerical EB modes (Figs. 12b,c) are also in some agreement with the theory (Fig. 12a). The difference between the patterns of the numerical and theoretical EB modes is due to the explicit momentum damping in the numerical EB mode, tending to suppress small-scale features in the interior ocean, which is particularly strong in the theoretical EB mode at larger latitudes.

Despite some similarities between the EB mode and the KB mode, there is a fundamental difference between them: the frequencies of the EB modes are determined by the basin zonal scale (appendix B), whereas the KB modes depend upon the basin perimeter. This can be seen through a set of experiments in which the latitudinal extent of the basin Y_N increases from 2000 to 8000 km (Fig. 13). Now, both the KB mode and EB mode closely follow the theoretical estimates, with the frequency of the first KB mode decreasing but the frequency of the first EB mode unchanged. This is also true for the higher KB modes and EB modes. Another difference between EB and KB modes is that, theoretically, the KB mode does not carry any potential vor-
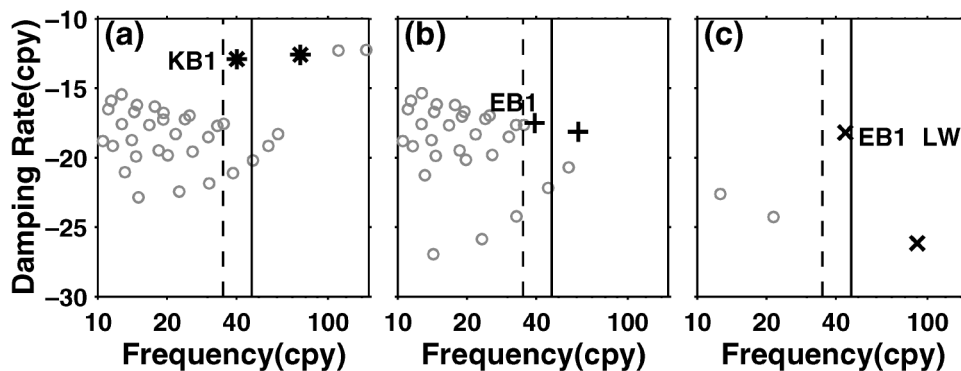

FIG. 11. Scatterplot of eigenvalues in the high-frequency regime for the KB and EB modes for (a) the standard case without any boundary blocking, (b) a basin with the northern boundary blocking, and (c) the case with long-wave approximation. The first two KB modes in (a) are highlighted by dark asterisks. The first two EB modes in (b) and (c) are highlighted by dark pluses and crosses, respectively. The dashed line and solid line label the frequency of the first KB and EB modes estimated from theory.
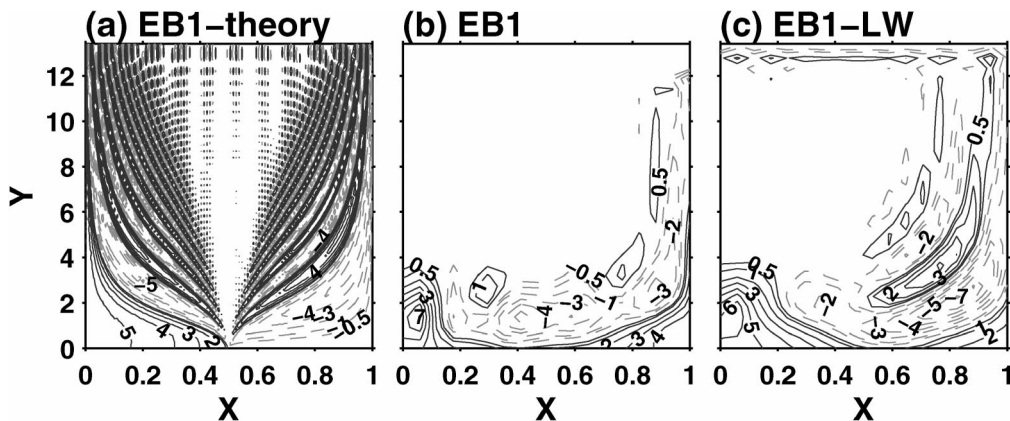
FIG. 12. Eigenstructures (real part of H) of the first EB modes obtained from (a) theory and (b), (c) our model; (b) is for the basin with the northern boundary blocked, and (c) is for the case with long-wave approximation. The basin size has been normalized by L_x in zonal direction and L_d in meridional direction.

ticity (PV) anomaly while the EB mode does. Our calculations of PV show that the KB mode carries very small PV anomaly because of boundary dissipation, while the EB modes carries much larger PV anomaly (figure not shown). This is well consistent with the theoretical prediction and could serve as one method to discriminate the EB and KB modes.

The EB modes can be also easily turned off in the numerical model by applying an extreme damping region on the western or eastern boundaries, or by assuming geostrophic balance in Eqs. (1a) and (1b). (In the latter case, the PB modes still exist as shown by CL.) In the cases with a partially blocked boundary, as in Fig. 6, the EB modes stand out, replacing the KB modes since the equatorial Kelvin and Rossby waves are not distorted. The structure of the first EB mode (not shown) is similar to that shown in Fig. 12b.

The discussions above seem to suggest an approximate relationship of the KB and EB mode as follows.
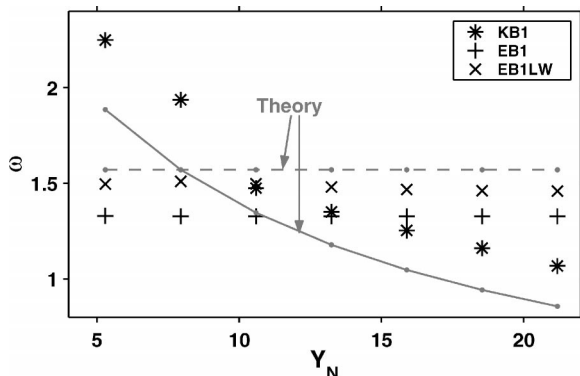

FIG. 13. Eigenvalues of the first numerical KB modes (asterisks), EB modes for the basin with the northern boundary blocked (pluses), and EB modes with long-wave approximation (crosses) for different northern boundary Y_N. The frequency of the first KB mode decreases with increasing Y_N while the frequency of the first EB mode keeps constant. The first theoretical KB mode (dot–solid line) and EB mode (dot–dashed line) are also plotted for comparison.

Overall, in a closed basin, the energy can be returned from the eastern to the western boundary via two routes. First, for a perfectly closed basin, the coastal Kelvin wave provides a main route to return energy from the east to the west, through its propagation around the basin perimeter. This allows the establishment of the KB mode, with temporal and spatial scales determined by the Kelvin wave propagating around the basin. This KB mode is valid even in a basin that does not include the equator, and can be seen in the example of midlatitude basin in Fig. 14. Second, when the equator is included in a basin, such as the tropical–extratropical basin, the westward reflection of equatorial Rossby wave provides an additional powerful and robust route that returns wave energy from the eastern to the western boundary. Nonetheless, if the closed basin is perfect such that the coastal Kelvin wave is allowed to circulate around the basin, the frequency and structure of the basin mode still appears to be determined primarily by the coastal Kelvin wave. Therefore, the basin mode is the KB mode, not the EB mode. However, if the basin is not perfect and if the coastal Kelvin wave route is distorted or suppressed in a more complicated basin, no Kelvin wave will be allowed to circulate around the basin. As a result, the KB mode disappears, whereas the EB mode stands out because the westward equatorial Rossby wave route occurs in the interior ocean and is robust. Despite the differences of the KB and EB modes, they appear to be equally important in the climate variability of the tropical–extratropical basin because, first, they both belong to a higher-frequency regime, relative to the PB mode discussed before, second, they have similar timescales since a realistic ocean basin has a zonal scale not much shorter than the meridional scale, and, third, they both have their energy concentrated in the equatorial waveguide and have similar spatial structure.

6. Summary and discussion

By solving the eigenvalue problem of a linear shallow-water system, the PB and KB modes in a closed
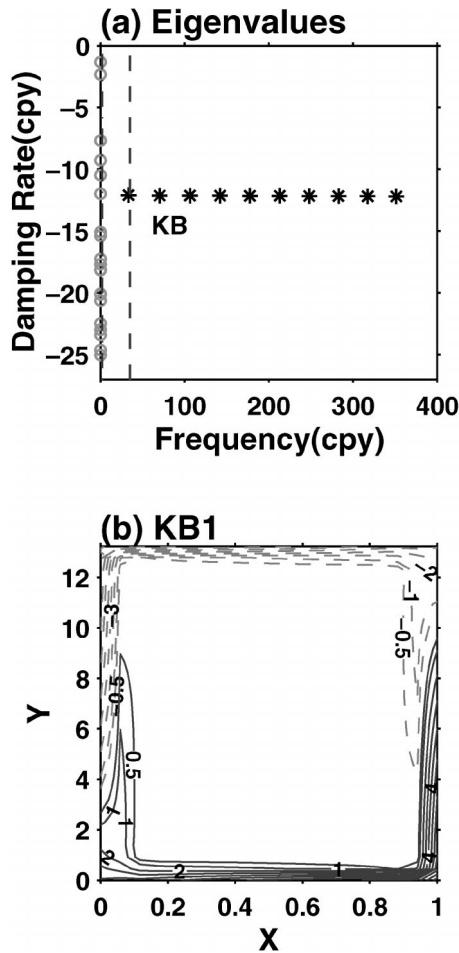
FIG. 14. Scatterplot of (a) eigenvalues for the experiment on an f plane and (b) the eigenstructure (real part of H) of the first KB mode. As compared with Fig. 1a, only Kelvin wave modes (highlighted by dark asterisks) can survive on an f plane.
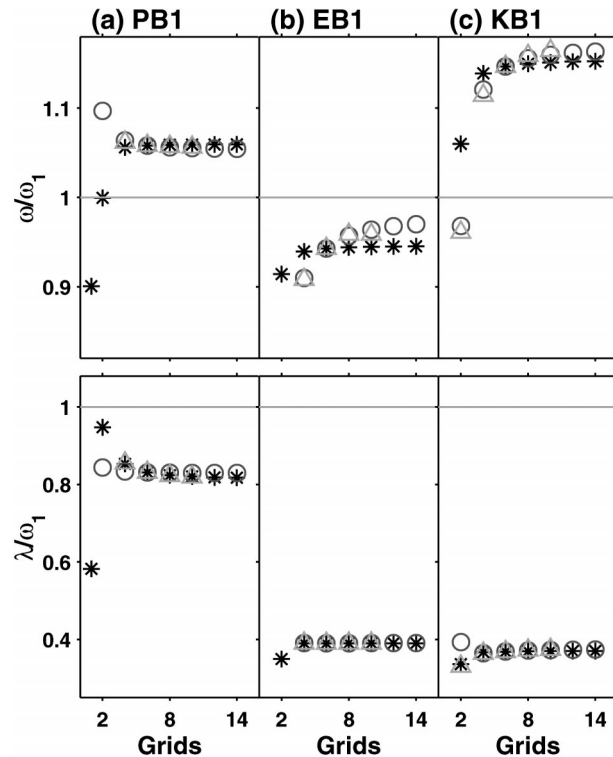

FIG. 15. (upper) Frequencies and (lower) damping rates of (a) the first PB, (b) EB, and (c) KB modes with increasing model resolution for a fixed basin of 3000 km × 5000 km normalized by theoretical ω_{P1}, ω_{E1}, and ω_{K1}, respectively. The x coordinate represents the number of grid points per 1000 km. The asterisks represent the first mode in the experiments with a fixed resolution in y direction (six grid points per 1000 km) and increasing resolution in x direction (denoted by x coordinate), the circles represent those with a fixed resolution in x direction (six grid points per 1000 km) and increasing resolution in y direction (denoted by x coordinate), and the triangles represent those with increasing resolution in both x and y directions simultaneously.

tropical–extratropical basin are identified, along with the EB modes in an infinite beta plane or under the long-wave approximation. These basin modes exhibit the strongest oscillatory nature because of the damping rates being much smaller than their corresponding frequencies. The PB modes are established after the extratropical planetary waves generated on the eastern boundary reach the western boundary. The KB modes are established after the coastal Kelvin waves travel one cycle around the basin, and the EB modes are established after the eastern boundary reflection of the eastward equatorial Kelvin waves hits the western boundary.

The major conclusions are not sensitive to the magnitude of model friction (not shown). However, it is critical for the PB mode that the damping in the mass equation be much smaller than the momentum damping, as pointed out by CL. The major conclusions are also insensitive to the model resolution. Figure 15 shows that the eigenvalues of the first PB, EB, and KB modes converge rapidly with the model resolutions. As the resolution increases, the frequencies of each mode finally approach a constant that deviates slightly from its corresponding theoretical value (the upper panels of Fig. 15). The damping rate shows a similar convergence with resolution. It is interesting to see that even rather coarse resolution can reproduce the eigenvalues of all the first basin modes very well. In general, the solutions for the first mode are sufficiently accurate when the resolution is about 200–300 km in both the x and y directions, comparable with the equatorial deformation radius (378 km). More specifically, the error range of the frequency of the numerical modes relative to the theoretical modes can be estimated from Fig. 15. The error is about +5% for the first PB mode, −4% for the first EB mode, and +16% for the first KB mode. That is, the numerical PB and KB modes tend to have higher frequency than their theoretical counterparts, while the numerical EB modes tend to have lower frequencies than the corresponding theoretical solutions. The discrepancies between numerical and theoretical modes may be more related to

the finite-difference scheme and the boundary conditions than the model resolution. Hsieh et al. (1983) have examined the free Kelvin wave in numerical models that employ the Arakawa B- or C-grid difference schemes. They found that the phase speed appears to be sensitive to the finite-difference schemes; the alongshore structure of the Kelvin wave appears much more seriously distorted in the B grid than in the C grid, while the offshore structure seems better behaved in the B grid than in the C grid. We will check the basin modes in a B grid model in our future work.

The KB mode seems to be vulnerable to coastal boundary conditions although this mode can exist in a perfectly closed basin. However, when the coastal Kelvin wave is suppressed somewhere along the boundary, the KB mode disappears. Instead, the EB mode emerges if the basin includes the equator. In principle, the EB mode differs from the KB mode in that the former depends on the basin zonal scale while the latter depends on the basin perimeter. However, for realistic major ocean basins in the Tropics–extratropics, the differences between the two may not be very important because, first, both modes have comparable frequencies at seasonal timescales and could equally contribute to equatorial interannual variability like ENSO and, second, they have most of their energy concentrated in the equatorial waveguide and similar spatial structures in the tropics, while the KB mode structure on the extratropical basin boundaries is not very important because of less energy there.

The PB modes can be affected by boundary perturbations. As such, the PB mode is determined by an effective basin boundary, rather than the geometric basin boundary. In a realistic ocean basin, however, it remains unclear where the effective basin boundary is located because the propagation of the coastal Kelvin wave can be distorted by the presence of a complex continental shelf, an open strait, or a frontal structure. For example, since the Australian continent extends to about 40°S, the PB mode in the Pacific and Indian Ocean will have the wave speed no longer than that at 40°S if the mode is determined by the southern boundary. As another example, the strong midlatitude frontal region between the subtropical and subpolar region may act as an effective basin boundary since the frontal zone with strong diapycnal mixing may distort the propagation of the low-frequency coastal Kelvin wave along the eastern boundary. While detailed examination of the effective basin boundary in a realistic basin is beyond the scope of this study, we can nonetheless make some inferences on the possible timescales of the PB modes from the available observations. The timescales of the PB modes are directly related to the planetary wave propagation speed, especially the first mode, which is rather insensitive to thermocline advection. The speed of these planetary waves has been estimated from the sea surface height (SSH) signal of the Ocean Topography Experiment (TOPEX)/Poseidon (T/P) data for global oceans
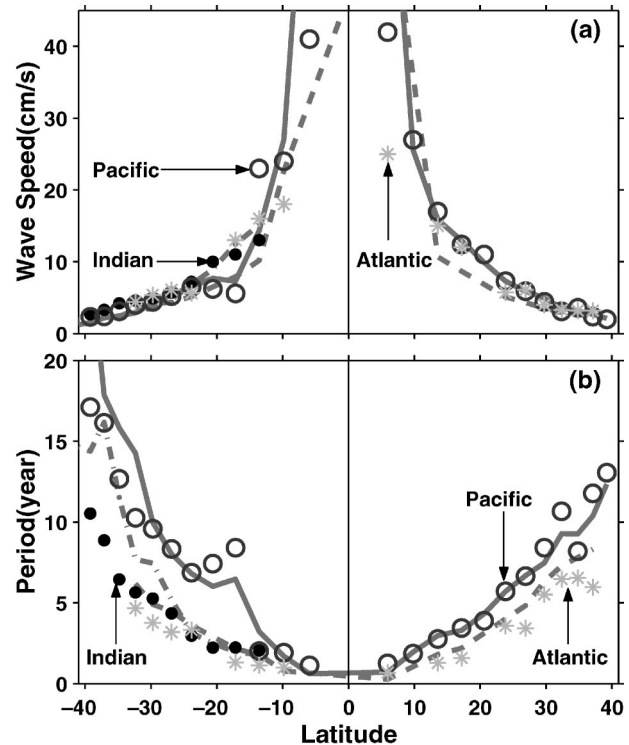

FIG. 16. The westward Rossby wave phase speed estimated from 7 years of (a) T/P data and corresponding Rossby wave cross-basin time (b). The open circles, asterisks, and solid circles correspond to estimates from the Pacific, the Atlantic, and Indian Oceans, respectively. The light solid lines, dashed line, and dot–dashed line indicate the predictions for the Pacific, the Atlantic, and Indian Oceans from the extended theory for extratropical freely propagating, nondispersive Rossby waves in the presence of the baroclinic background mean flow (Chelton et al. 1998).

(Fig. 16a) (Fu and Chelton 2001). These wave speeds are then used to calculate cross-basin time of Rossby waves at different latitudes (Fig. 16b). It is seen that, at the highest latitudes from observations (at midlatitude about 40°), the cross-basin time is about 15 years for the Pacific (circles) and up to 10 years for Atlantic and Indian Oceans. Therefore, if the effective basin boundaries in these oceans extend to the midlatitude, the PB modes could have decadal timescales.

APPENDIX A

The Numerical Eigenvalue Model

a. Numerical scheme for eigenvalue problem

The eigenvalue problem (4) is solved numerically by approximating matrix L with a finite difference in C

grid. Suppose h has n and m grid points in x and y directions, respectively, and we have the discrete array $h = h[1{:}n, 1{:}m]$, $u = u[1{:}n - 1, 1{:}m]$, and $v = v[1{:}n, 1{:}m - 1]$. The finite-difference form of (4) is then

$$i\sigma u_{ij} = M\delta_u u_{ij} - \frac{y_{uj}}{4}(v_{ij-1} + v_{i+1j-1} + v_{ij} + v_{i+1j})$$

$$+ \frac{1}{\Delta x_{ij}}(h_{i+1j} - h_{ij}), \qquad (A1a)$$

$$i\sigma v_{ij} = \frac{M^2 y_{vj}}{4}(u_{i-1j} + u_{i-1j+1} + u_{ij} + u_{ij+1}) + M\delta_v v_{ij}$$

$$+ \frac{M^2}{\Delta y_{ij}}(h_{ij+1} - h_{ij}), \quad \text{and} \qquad (A1b)$$

$$i\sigma h_{ij} = \frac{1}{\Delta x_{ij}}(u_{ij} - u_{i-1j}) + \frac{1}{\Delta y_{ij}}(v_{ij} - v_{ij-1}) + M\delta_{ij} h_{ij},$$
$$\qquad (A1c)$$

where Δx_{ij} and Δy_{ij} are grid sizes in x and y directions, respectively. Rearranging terms in (A1) in the order of u, v, h and $\ldots$, $i - 1$, i, $i + 1$, $\ldots$, $j - 1$, j, $j + 1$, $\ldots$, we have

$$i\sigma u_{ij} = A_u u_{ij} + C_{uj} v_{ij-1} + C_{uj} v_{i+1j-1} + C_{uj} v_{ij}$$

$$+ C_{uj} v_{i+1j} + D_{xij} h_{ij} - D_{xij} h_{i+1j}, \qquad (A2a)$$

$$i\sigma v_{ij} = C_{vj} u_{i-1j} + C_{vj} u_{ij} + C_{vj} u_{i-1j+1} + C_{vj} u_{ij+1}$$

$$+ A_v v_{ij} + M^2 D_{yij} h_{ij} - M^2 D_{yij} h_{ij+1}, \qquad (A2b)$$
and

$$i\sigma h_{ij} = D_{xij} u_{i-1j} - D_{xij} u_{ij} + D_{yij} v_{ij-1} - D_{yij} v_{ij}$$

$$+ A_h h_{ij}. \qquad (A2c)$$

Here,

$$(A_u, A_v, A_h) = M(\delta_u, \delta_v, \quad \delta_h),$$

$$C_{uj} = -\frac{y_{uj}}{4}, \qquad C_{vj} = \frac{M^2 y_{vj}}{4},$$

$$D_{xij} = -\frac{1}{\Delta x_{ij}}, \quad \text{and} \quad D_{yij} = -\frac{1}{\Delta y_{ij}}.$$

The finite-difference forms of the no-normal flow condition for u and v are

$$u_{1j} = u_{nj} = 0 \quad \text{and} \quad v_{i1} = v_{im} = 0. \qquad (A3)$$

The number of equations for u, v, and h are $(n - 1) \times m$, $n \times (m - 1)$, and $n \times m$, respectively. Therefore, the size of the coefficient matrix **L** in (4) is $[3 \times m \times n - m - n] \times [3 \times m \times n - m - n]$, and the number of eigenvalues σ is $3 \times m \times n - m - n$. Since we are interested in the complete eigenspectrum of basin modes, we use Matlab function $[V, \sigma] = \text{eig}(L)$ to find all of the eigenvalues (see online at http://www.mathworks.com/access/helpdesk/help/techdoc/ref/eig.shtml for details), where V is a full matrix whose columns are the

corresponding eigenvectors of eigenvalues σ. Because of computational limitations, most of the calculations use $n = 18$ and $m = 30$ for a basin of 3000 km $\times$ 5000 km. The corresponding model resolution 167 km is smaller than the equatorial deformation radius (378 km). Sensitivity studies with different resolutions (see Fig. 15 for mode 1) show that the model resolution is not crucial to the large-scale basin modes provided that it is smaller than the deformation radius. In this paper, we set the model southern boundary on the equator to focus on the hemispherically symmetric modes.

b. Extreme damping region

Excessive damping is added in specific extreme damping regions to suppress wave propagation in the eigenvalue problem. Specifically, in the damping region extremely large δ_u, δ_v, and δ_h are applied. It is important to point out that the δ_h is applied the same large value as the δ_u, δ_v in the damping region to ensure true damping or blocking of the signal at all the scales. The extreme damping region acts like a "black hole" to absorb any incoming signal. As seen in the text, this damping region provides a useful way to study wave mechanisms in the eigenvalue problem.

c. "Long-wave approximation"

For convenience, an approximate "long-wave approximation" is used in the numerical model. Equation (1b) is subsequently rewritten as

$$v_t + M^2(yu + h_y + \delta_v v) = 0. \qquad (A4)$$

By giving a very large $M = L_x/L_d$, the local acceleration term v_t becomes negligible, which gives the long-wave approximation with small damping. Physically, our long-wave approximation is similar to a very long basin ($L_x \gg L_d$). Sensitivity tests show that the results are insensitive to the magnitude of δ_v. The finite-difference form of (A4) after use of the long-wave approximation is

$$i\sigma v_{ij} = M\left[\frac{y_{vj}}{4}(u_{i-1j} + u_{i-1j+1} + u_{ij} + u_{ij+1})\right.$$

$$\left. + \delta_v v_{ij} + \frac{1}{\Delta y_{ij}}(h_{ij+1} - h_{ij})\right]. \qquad (A5)$$

APPENDIX B

Theoretical Solutions

The theoretical solutions have been derived previously (CL; Jin 2001; LIU). Here, they are described briefly for the sake of completeness.

a. Planetary wave model solution

The PB modes can be derived from the planetary wave model (CL; LIU). Assuming Eqs. (1a) and (1b)

are in geostrophic balance, the eigenfunction satisfying the eastern boundary condition ($u|_{x=1} = 0$) in nondimensional form is

$$H = e^{[\sigma_P(x-1)y^2]}. \qquad (B1)$$

The eigenvalue $\sigma_P = \lambda_P + i\omega_P$ is determined by mass conservation condition (2) as

$$\int_{Y_S}^{Y_N} \frac{(1 - e^{-\sigma_P y^2})}{y^2} \, dy = 0, \qquad (B2)$$

where Y_S and Y_N are the basin southern and northern boundaries, respectively. Here, we have set $Y_S = 0$, on the equator, to focus on the symmetric modes. Equation (B2) has infinite eigenvalues $\sigma_{Pj} = \lambda_{Pj} + i\omega_{Pj}(j = 0, 1, 2, \ldots, \infty)$. For $Y_N > O(1)$, the frequencies can be approximated as $\omega_{Pj} = j\omega_P$, where the fundamental frequency ω_{P1} corresponds to the cross-basin time of the slowest planetary wave along the northern boundary, Y_N. The nondimensional planetary wave speed at the northern boundary is given as $c_N = 1/Y_N^2$ and so

$$\omega_{P1} = 2\pi/Y_N^2. \qquad (B3)$$

All the eigenvalues are damped ($\lambda_{Pj} < 0$) except for the trivial solution $\sigma_{P0} = 0$.

b. Equatorial wave model solutions

The PB and EB modes can also be derived from the equatorial wave model (Jin 2001; LIU). After the long-wave approximation in Eq. (1b), we have the solution that satisfies the solid wall eastern boundary condition as $h = H(x, y)e^{\sigma i}$, where $H = (q + p)/2$ and

$$q_{j,k}(x, y) = \sum_{n=0}^{N} q_{2n}(x)\psi_{2n}(y),$$

$$p_{j,k}(x, y) = \sum_{n=0}^{N-1} p_{2n}(x)\psi_{2n}(y), \qquad (B4)$$

$$q_{2n}^{j,k} = \sqrt{(2n - 1)!!/(2n)!!} \times e^{\{\sigma_{j,k}[4n(x-1)-x]\}},$$

and

$$p_{2n}^{j,k} = \sqrt{(2n + 2)/(2n + 1)}q_{2n+2}^{j,k}. \qquad (B5)$$

Here, $\psi_{2n}(y)(n = 0, 1, 2, \ldots)$ is hyperbolic cylindrical function (cf. Battisti 1988) and $\sigma = \lambda + i\omega$ is the eigenvalue. With no net transport across the western

boundary $\int_{-\infty}^{\infty} u|_{x=0} \, dy = 0$, the above solution leads to the eigenvalue problem of

$$1 - \sum_{n=1}^{N} \frac{(2n - 3)!!}{(2n)!!} e^{-4\sigma} = 0. \qquad (B6)$$

The eigenvalues can also be expressed approximately as (see details in Jin 2001)

$$\sigma_{j,k} = [-(\ln\rho_j - ij2\pi/N) \pm ik2\pi]/4,$$

$$j = 0, 1, \ldots, N - 1; \qquad k = 0, 1, 2, \ldots, \quad (B7)$$

where k is the node number of the eigenfunction along the equator. The fundamental frequency for the equatorial wave modes, based on (B7), is $\omega_{0,1} = \pi/2$, as derived previously by CM.

REFERENCES

Battisti, D. S., 1988: The dynamics and thermodynamics of a warming event in a coupled tropical atmosphere–ocean model. *J. Atmos. Sci.,* **45,** 2889–2919.

Cane, M., and D. Moore, 1981: A note on low-frequency equatorial basin modes. *J. Phys. Oceanogr.,* **11,** 1578–1584.

Cessi, P., and S. Louazel, 2001: Decadal oceanic response to stochastic wind forcing. *J. Phys. Oceanogr.,* **31,** 3020–3029.

——, and F. Primeau, 2001: Dissipative selection of low-frequency modes in a reduced-gravity basin. *J. Phys. Oceanogr.,* **31,** 127–137.

Chelton, D. B., R. A. de Szoeke, M. G. Schlax, K. El Naggar, and N. Siwertz, 1998: Geographical variability of the first-baroclinic Rossby radius of deformation. *J. Phys. Oceanogr.,* **28,** 433–460.

Fu, L.-L., and D. B. Chelton, 2001: Large-scale ocean circulation. *Satellite Altimetry and Earth Sciences,* L.-L. Fu and A. Cazenave, Eds., Academic Press, 131–169.

Hsieh, W. W., M. K. Davey, and R. C. Wajsowicz, 1983: The free Kelvin wave in finite difference numerical models. *J. Phys. Oceanogr.,* **13,** 1383–1397.

Jin, F. F., 2001: Low-frequency modes of tropical ocean dynamics. *J. Climate,* **14,** 3874–3881.

Liu, Z., 2002: How long is the memory of tropical ocean dynamics? *J. Climate,* **15,** 3518–3522.

——, 2003: Tropical ocean decadal variability: Resonance of planetary wave basin modes. *J. Climate,* **16,** 1539–1550.

——, L. Wu, and E. Bayler, 1999: Rossby wave–coastal Kelvin wave interaction in the extratropics. Part I: Low-frequency adjustment in a closed basin. *J. Phys. Oceanogr.,* **29,** 2382–2404.

Milliff, R. F., and J. C. McWilliams, 1994: The evolution of boundary pressure in ocean basins. *J. Phys. Oceanogr.,* **24,** 1317–1338.

Moore, D., 1968: Planetary–gravity waves in an equatorial ocean. Ph.D. thesis, Harvard University, 207 pp.

Primeau, F., 2002: Long Rossby wave basin-crossing time and the resonance of low-frequency basin modes. *J. Phys. Oceanogr.,* **32,** 2652–2665.